

Control of submillisecond synaptic timing in binaural coincidence detectors by K_v1 channels

Paul J Mathews^{1,4}, Pablo E Jercog^{2,4}, John Rinzel^{2,3}, Luisa L Scott¹ & Nace L Golding¹

Neurons in the medial superior olive process sound-localization cues via binaural coincidence detection, in which excitatory synaptic inputs from each ear are segregated onto different branches of a bipolar dendritic structure and summed at the soma and axon with submillisecond time resolution. Although synaptic timing and dynamics critically shape this computation, synaptic interactions with intrinsic ion channels have received less attention. Using paired somatic and dendritic patch-clamp recordings in gerbil brainstem slices together with compartmental modeling, we found that activation of K_v1 channels by dendritic excitatory postsynaptic potentials (EPSPs) accelerated membrane repolarization in a voltage-dependent manner and actively improved the time resolution of synaptic integration. We found that a somatically biased gradient of K_v1 channels underlies the degree of compensation for passive cable filtering during propagation of EPSPs in dendrites. Thus, both the spatial distribution and properties of K_v1 channels are important for preserving binaural synaptic timing.

The temporal relationship between excitatory synaptic input and action potential output is critical for sensory encoding as well as for the induction of some forms of synaptic plasticity^{1,2}. However, in the majority of neurons in which excitatory inputs sum in the dendritic arbor, the relative timing of synaptic input is subject to distortions in both time and amplitude as a result of dendritic cable filtering^{3,4}. The computational challenge of maintaining fine temporal resolution in the face of dendritic distortions is especially acute in neurons of the medial superior olive (MSO) in which phase-locked auditory information from the two ears is first integrated. Principal neurons of the MSO encode microsecond differences in the arrival time of sounds to the two ears (interaural time differences, or ITDs) through systematic variations in the rate of action potential output. Rate-encoded ITDs are a critical cue used by birds and mammals for localizing sounds along the horizontal plane^{5–7}.

At the cellular level, discrimination of ITDs in mammals involves the spatial and temporal summation of time-locked glutamatergic excitation and glycinergic inhibition in MSO principal neurons. Excitatory synaptic inputs from spherical bushy cells of the cochlear nucleus are segregated onto different branches of bipolar dendritic arbors⁸. The axon, where action potential initiation occurs, emerges from the soma or proximal dendrite^{9,10}. Although computational models have been used to predict that this synaptic input segregation in MSO neurons and their avian analogs may improve the fidelity of binaural coincidence detection^{11–14}, there has been almost no experimental data to date regarding the dendritic properties of these cells, and the role of the dendrites in shaping binaural coincidence detection is therefore unclear.

To understand how MSO dendrites influence synaptic coincidence detection, we combined simultaneous dendritic and somatic

current-clamp recordings, both whole-cell and excised patch voltage-clamp recordings, and computational modeling to explore how the properties of MSO dendrites influence binaural coincidence detection and temporal coding. We found that dendritic EPSPs activated a somatically biased population of low voltage-activated K^+ channels (K_{LVA}), which accelerated membrane repolarization. The presence of K_{LVA} approximately doubled the temporal resolution of binaural coincidence detection as compared with a passive leak conductance of the same density and imposed a uniform somatic time course of EPSPs propagating from disparate dendritic locations. Thus, both the biophysical properties and spatial distribution of K_{LVA} are critical determinants of the high resolution of binaural coincidence detection in the MSO.

RESULTS

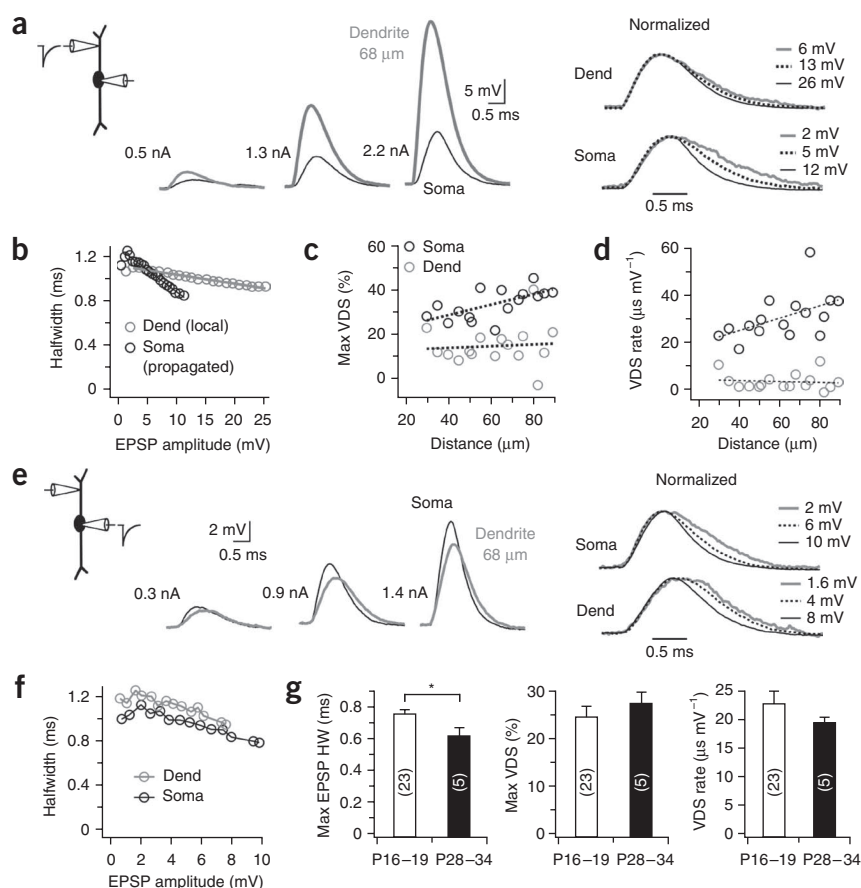
MSO principal cells were identified in brainstem slices by the bipolar morphology of their dendrites when viewed under infrared differential interference contrast optics⁹, and by the characteristic onset (single spike) firing pattern and unusually low input resistance these cells exhibit electrophysiologically (average of $12.0 \pm 0.69 \text{ M}\Omega$ for postnatal day 16–19 (P16–19) gerbils, $n = 20$). To examine how EPSPs are shaped as they propagate from known locations in the dendrites to the soma, we made simultaneous somatic and dendritic current-clamp recordings, injected simulated excitatory postsynaptic currents (sEPSCs, see Online Methods) into the dendrites and varied current amplitude to elicit depolarizations encompassing the entire subthreshold voltage range (Fig. 1a). These simulated EPSPs (sEPSPs) showed marked attenuation following propagation to the soma, which was proportional to the recording distance. In all of the recordings, one of the most notable features of sEPSPs was the voltage dependence

¹Section of Neurobiology and Institute for Neuroscience, University of Texas at Austin, Austin, Texas, USA. ²Center for Neural Science, New York University, New York, New York, USA. ³Courant Institute of Mathematical Sciences, New York University, New York, New York, USA. ⁴These authors contributed equally to this work. Correspondence should be addressed to N.L.G. (golding@mail.utexas.edu).

Received 15 December 2009; accepted 8 March 2010; published online 4 April 2010; doi:10.1038/nn.2530

Figure 1 Propagation of simulated EPSPs from the dendrites to the soma in MSO neurons.

(a) Simultaneous recording from the soma (black) and dendrite (gray) in response to injection of dendritic sEPSCs of three increasing amplitudes (0.2, 0.8 and 2.2 nA). The sEPSPs are shown normalized at the right, revealing a systematic decrease in sEPSP halfwidth with increasing amplitude. (b) Plot of halfwidth versus sEPSP amplitude for the cell shown in a, revealing a steeper VDS of sEPSPs at the soma versus the dendrite. (c) Population data indicated that the maximum degree of VDS was more prominent at the soma than in the dendrites. There was a trend for stronger VDS at both recording sites with increasing distance from the soma (0.06% per μm dendrite, 0.20% per μm soma, $n = 16$). (d) The rate of VDS over the subthreshold voltage range was higher at the soma than at the dendrite (fits: dendrite, $0.02 \pm 0.05 \mu\text{s mV}^{-1} \mu\text{m}^{-1}$; soma, $0.26 \pm 0.12 \mu\text{s mV}^{-1} \mu\text{m}^{-1}$). (e, f) Attenuation of backpropagating sEPSPs in the cells shown in a and b was far less pronounced than during forward propagation from the dendrites to the soma. Note the prominent VDS observed in normalized traces with somatic sEPSC injection (e, right). (g) VDS was insensitive to developmental stage. Despite a significant decline in EPSP duration (minimum halfwidth, measured just below spike threshold, $P = 0.03$), VDS magnitude and rate in electrophysiologically mature gerbils (P28–34) was not significantly different from that in younger gerbils (P16–19, $P = 0.43$ and $P = 0.21$ for magnitude and rate, respectively).



of their shape. As the amplitude of sEPSPs increased, their halfwidth (sEPSP duration measured at half amplitude) progressively declined in both the dendrite and soma, contrary to what would be observed in a passive system in which EPSP halfwidth is independent of amplitude (Fig. 1a,b). We defined the maximum voltage-dependent sharpening (VDS), as the percentage decrease in halfwidth (HW) observed in a family of sEPSPs spanning the subthreshold voltage range, from ~1–2 mV

to just below spike threshold ($\frac{HW_{\min \text{ EPSP}} - HW_{\max \text{ EPSP}}}{HW_{\min \text{ EPSP}}} \cdot 100\%$).

The maximum VDS differed at the two recording locations. The average maximum VDS was 35% at the soma, but only 15% in the dendrites, despite the fact that the dendrites received far greater depolarizations (Fig. 1c). Because VDS is sensitive to the magnitude of the subthreshold voltage range, which varied across cells from 8–19 mV, we normalized VDS for each family of sEPSPs with respect to the

sEPSP amplitude (VDS rate = $\frac{\max \Delta HW}{\max \Delta A}$, with A being amplitude;

Fig. 1d). VDS rates averaged $31.0 \mu\text{s mV}^{-1}$ at the soma, but were only $3.9 \mu\text{s mV}^{-1}$ at the site of sEPSC injection in the dendrites (30–90 μm , $n = 16$). Both the rate and magnitude of VDS in the dendrites were insensitive to the site of dendritic sEPSC injection, whereas VDS tended to increase proportionally with sEPSC injection distance for propagated sEPSPs measured at the soma (Fig. 1c). Presumably, the voltage-dependent mechanism responsible for EPSP sharpening is more effectively recruited by the large dendritic EPSPs that are necessary for the production of comparable somatic sEPSP amplitudes.

These results indicate that the mechanism underlying the shortening of sEPSP duration is particularly prominent in the perisomatic region. Accordingly, when sEPSCs were injected into the soma in the same population of cells, we observed a prominent voltage dependence of sEPSP duration at the soma even in the absence of strong dendritic depolarization (25% maximal sharpening over the 12-mV average subthreshold voltage range at the soma, $n = 17$; Fig. 1e,f). In these responses, there was also a marked asymmetry in the attenuation of sEPSPs propagating toward the soma relative to those backpropagating into the distal dendrites (Fig. 1a,e). Further refinement of backpropagating sEPSP duration in the dendrites was detected, but was relatively subtle (Fig. 1f). Finally, given that the intrinsic electrical properties of MSO principal cells are known to undergo developmental changes up to ~3 postnatal weeks⁹, we measured VDS in MSO neurons recorded from gerbils between P28–34. Although sEPSP halfwidths were narrower in older than in younger neurons (0.62 ± 0.04 ms versus 0.76 ± 0.02 ms, $n = 5$ and 23, respectively; $P = 0.03$), VDS rate and maximum magnitude were not significantly different between the two age ranges ($P = 0.43$ and 0.21 for max VDS and VDS rate, respectively; Fig. 1g). Thus, VDS appears to be relatively insensitive to developmental stage.

To understand how EPSP shape is controlled as a function of distance in the dendrites, we compared the somatic shape of the maximal subthreshold sEPSPs that had been introduced into the soma itself (in dual somatic recordings, $n = 12$) or into different locations along the dendrites ($n = 16$; Fig. 2). Comparable somatic depolarizations required progressively larger dendritic sEPSPs to overcome the large attenuation observed during propagation in MSO dendrites (Fig. 2a). However, somatic sEPSPs appeared to be relatively uniform in rise

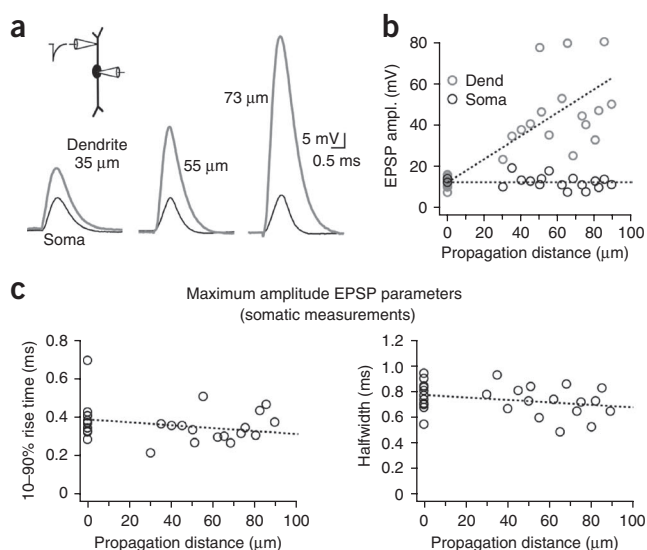


Figure 2 The shape of EPSPs is stable regardless of propagation distance. **(a)** sEPSPs from different dual dendritic and somatic recordings elicited with sEPSCs adjusted to be just below action potential threshold. Increasing dendritic depolarizations were required as a function of distance to produce just subthreshold somatic sEPSPs of comparable amplitude and shape (amplitude of current injections: 2.3, 3.2 and 2.8 nA for dendritic recordings; 35, 55 and 73 μm from the soma). **(b)** Group data from all paired recordings showing dendritic responses (gray circles) and somatic responses (black circles). Points at 0 μm: sEPSP responses to somatic current injection were obtained using dual somatic recordings to prevent distortions of shape as a result of series resistance. **(c)** Rise time and halfwidth of maximal subthreshold sEPSPs (recorded at the soma) as a function of the sEPSC dendritic location. sEPSPs at the soma propagating from different dendritic locations were of comparable rise time and duration as those elicited locally at the soma. Linear fits to the data indicate a slight negative trend with increasing distance from the soma (dotted lines). Linear fits have slopes of -0.001 ms/μm and are constrained to pass through the average somatic responses at 0 μm (rise time, 0.39 ms; halfwidth, 0.77 ms).

time and duration despite their different spatial origins (**Fig. 2c**). These results suggest that VDS compensates for EPSP broadening from passive cable properties of the dendrite, which would be expected to prolong both the rise time and the decay of sEPSPs originating from more distal dendritic locations.

A candidate mechanism that could contribute to VDS is a fast-activating K_{LVA} conductance that has been described in several auditory and nonauditory neurons, including principal cells of the MSO. These K^+ channels are composed of subunits from the K_v1 subfamily, and have been shown to influence membrane excitability in the subthreshold voltage range^{9,15}. To test whether these channels are capable of influencing the repolarization of propagating EPSPs in the MSO, we examined the effects of α -dendrotoxin (DTX), a potent blocker of the $K_v1.1, 1.2, 1.3$ and 1.6 subunits, on subthreshold EPSP shape in the soma and dendrites. Bath application of 100 nM DTX produced marked changes in the intrinsic properties of MSO cells. VDS was strongly affected by DTX. When maximal subthreshold somatic sEPSPs were generated via dendritic sites 55–90 μm away (propagated sEPSPs), VDS was largely eliminated (from 39% to 8% in the presence

of DTX, $n = 4$; **Fig. 3a–c**). When sEPSPs were both generated and measured at the soma in dual recordings (local sEPSCs), K_{LVA} blockade not only eliminated VDS, but induced a voltage-dependent broadening in some cells (average VDS changed from 27% to -18% , $n = 5$; **Fig. 3d**). The latter effect reflects the activation of voltage-gated sodium channels by sEPSPs that is normally masked by K^+ channel activation¹⁶. The effects of DTX on EPSPs were partially the result of changes in resting conductances. In the presence of DTX, the resting potential depolarized by ~ 3 mV (-61.7 ± 1.4 to -58.4 ± 1.3 mV, $P = 0.007$) and the input resistance measured at the soma increased by approximately threefold (11.4 ± 1.3 to 36.2 ± 4.2 MΩ, $P = 0.0003$,

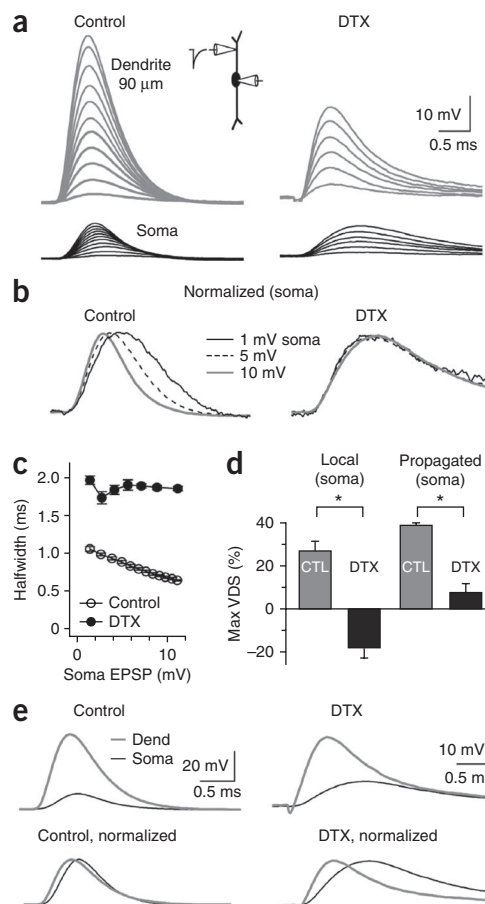


Figure 3 A DTX-sensitive conductance mediates EPSP sharpening. **(a)** Simultaneous dendritic (gray) and somatic (black) voltage responses to sEPSCs recorded in control ACSF and in the presence of 100 nM DTX. sEPSCs were injected into the lateral dendrite 90 μm from the soma (0.2–2.2 nA, 0.2-nA increment). In DTX, sEPSP attenuation was sharply reduced and both the rise time and duration of the response was increased (sEPSC, 0.2–1.2 nA, 0.2-nA increment). **(b)** Normalized traces of three selected sEPSPs in **a** showing VDS over the subthreshold voltage range. sEPSPs of identical amplitude exhibited no VDS in DTX (right). **(c)** In the neuron shown in **a**, DTX eliminated VDS and increased sEPSP halfwidth by about twofold. Points are the average of five traces. **(d)** Group data showing VDS at the soma in response to somatic sEPSCs (local, $n = 5$) or in the dendrite 55–90 μm away (propagated, $n = 4$). Local sEPSPs at the soma were generated and measured using different pipettes in dual recordings. Maximum VDS (max VDS) was expressed for EPSP halfwidth in control ACSF (gray bars) and in the presence of DTX (black bars). Negative and positive values reflect a relative broadening and sharpening, respectively. Asterisks indicate significant differences between control and DTX conditions (paired two-tailed t test; $P = 0.0004$ and $P = 0.0002$ for local and propagated sEPSPs, respectively). **(e)** DTX slowed the rise time and increased the duration of sEPSPs during propagation from the dendrites to the soma, 90 μm away (same cell shown in **a–c**). Control, 2,200 pA; DTX, 1,200 pA.

Figure 4 Characterization of I_{K-LVA} in outside-out patches.

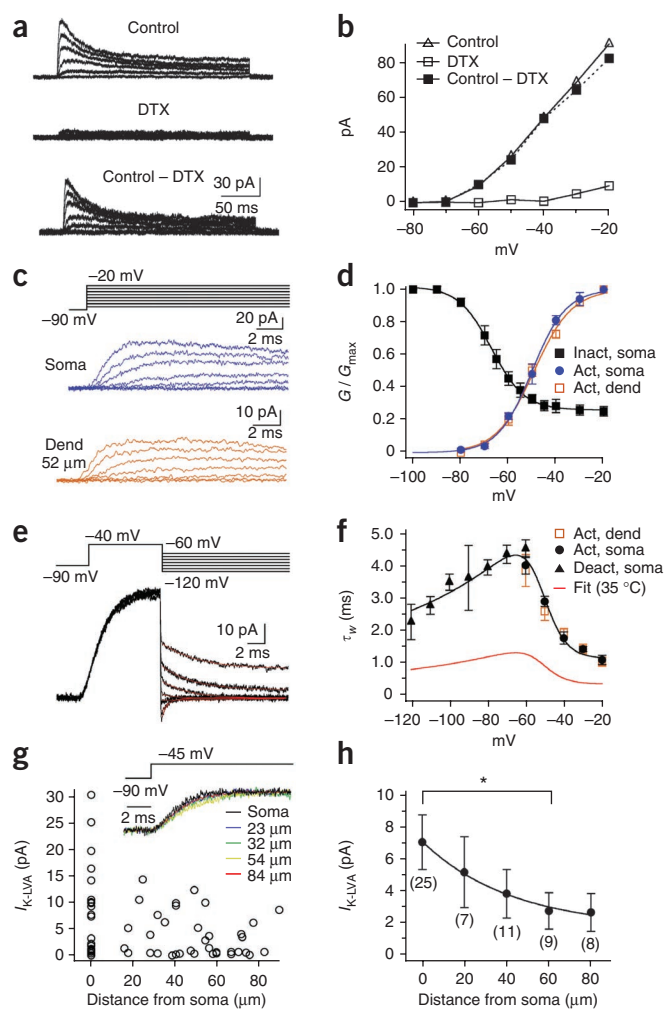
(a,b) Pharmacologically isolated I_{K-LVA} during voltage clamp. Voltage was stepped from -90 mV to potentials between -80 to -20 mV in 10 -mV increments. Outward currents resistant to 100 nM DTX (middle) were subtracted from control (top), yielding the DTX-sensitive current (bottom). (c) Kinetic similarity of DTX-sensitive currents recorded at the soma and dendrites. Voltage steps were the same as in a. (d) Activation and steady-state inactivation of I_{K-LVA} . The peak conductance of DTX-sensitive K^+ channels in the soma (blue) and dendrites (brown) elicited by steps between -80 and -20 mV from -90 mV. Steady-state inactivation of somatic I_{K-LVA} : peak conductances from voltage steps to -45 mV from a -90 -mV holding potential after 1.5 -s prepulses between -120 and -30 mV ($n = 6$; **Supplementary Fig. 1**). (e) Deactivation of I_{K-LVA} . Prepulses (-90 to -40 mV for 10 ms) followed by tail currents elicited between -60 and -120 mV. Fits were made to tails 300 μ s to 15 ms after the step (see Online Methods). (f) Activation and deactivation rates (τ_w) versus voltage for somatic patches (blue circles and triangles, respectively). Activation rates are shown for dendritic patches (brown). Fits to τ_w at 25°C were made according to

$$f(V) = 0.28 \left(100 / \left(6e^{\frac{V+60}{6.34}} + 24e^{\frac{V+60}{63.53}} \right) \right) + 1.23, \text{ also shown adjusted to}$$

35°C using an experimentally measured Q_{10} of 3.3 (red). (g) Distribution of I_{K-LVA} in the soma and dendrites. Inset, normalized peak currents from different locations have similar kinetics. (h) Average current amplitude at the soma and dendrite (20 - μ m bins) decreased with a length constant of 42 μ m (single exponential fit). Dendritic currents in the 60 - μ m bin were significantly different from those at the soma (*; $P = 0.41, 0.06, 0.03$ and 0.06 for bins 20 – 80 μ m, respectively, Wilcoxon signed rank test, unequal sample variances).

$n = 7$), indicating that K_{LVA} contributes to the resting conductance of MSO principal neurons. The increase in input resistance also decreased the somatic current required to generate action potentials by 3.3 -fold ($2,060 \pm 921$ to 620 ± 277 pA, $n = 5$). Finally, blockade of K_{LVA} strongly affected the cable-filtering properties of MSO dendrites (**Fig. 3e**). sEPSPs propagating from the distal dendrites (55 – 90 μ m) to the soma were sharpened by 19% in normal artificial cerebrospinal fluid (ACSF, 0.79 ± 0.10 ms in dendrites versus 0.61 ± 0.05 ms in soma, $n = 4$), but were broadened by 92% when DTX was added (1.25 ± 0.14 ms in dendrites versus 2.36 ± 0.40 ms in soma). These results indicate that DTX-sensitive K^+ channels are critical for reducing the temporal broadening of synaptic excitation that would otherwise occur if the dendrites were passive.

To directly observe the DTX-sensitive currents, we made voltage-clamp recordings of pharmacologically isolated K^+ currents in outside-out patches pulled from both the soma and dendrites of MSO principal cells (25°C ; **Fig. 4**). These procedures allowed us to record the voltage sensitivity and activation kinetics of these currents under conditions of high spatial and temporal voltage control. Patches were held at -90 mV to remove inactivation and then stepped to voltages between -80 and -20 mV in 10 -mV increments (**Fig. 4a–c**). These step commands evoked fast activating, slowly inactivating currents at voltages positive to -70 mV. Outward currents exhibited both inactivating and non-inactivating components, both of which were extensively blocked in the presence of 100 nM DTX ($77 \pm 8\%$ blockade at -40 mV, $n = 6$; **Fig. 4a,b**). The half-activation voltage was similar for both somatic and dendritic patches (somatic, -49.0 ± 1.5 mV, slope of 7.4 ± 0.7 mV; dendritic, -48.8 ± 1.4 mV, slope of 8.1 ± 0.4 mV; **Fig. 4c,d**). We measured steady-state inactivation of K_{LVA} current (I_{K-LVA}) in somatic patches with prepulses between -100 and -20 mV for 1.5 s followed by a test pulse to -45 mV for 200 ms (**Supplementary Fig. 1**). The inactivating component of I_{K-LVA} comprised 74% of the total current and showed a half-inactivation voltage of -67.1 ± 1.5 mV, with a slope



factor of -6.2 ± 0.5 mV ($n = 6$; **Fig. 4d**). I_{K-LVA} in both the soma and dendrite displayed fast, nearly identical activation kinetics; when corrected for an experimentally measured temperature coefficient (Q_{10}) of 3.3 , activation time constants decreased from 1.32 to 0.33 ms between -60 and -20 mV (**Fig. 4c,f**). Deactivation of I_{K-LVA} following brief voltage steps in somatic patches was also rapid, ranging from 1.37 to 0.69 between -60 and -120 mV (**Fig. 4e,f**). Finally, we examined the somatodendritic distribution of I_{K-LVA} in outside-out patches pulled from either the soma or dendrites up to 90 μ m away (**Fig. 4g,h**). In response to steps from -90 to -45 mV, I_{K-LVA} kinetics were similar in patches all along the soma and dendrites (**Fig. 4g**). However, current amplitude was, on average, lower in the dendrites relative to the soma (**Fig. 4h**). The average amplitude of I_{K-LVA} declined systematically as a function of distance along the dendrites. I_{K-LVA} averaged 7.06 ± 1.7 pA at the soma and decreased to 2.7 ± 1.18 pA in the dendrites up to 90 μ m in the dendrites ($n = 24$ for soma, $n = 37$ for dendrite, 20 - μ m bins; **Fig. 4h**). Thus, I_{K-LVA} is available for activation by EPSPs throughout MSO neurons, but its density is substantially biased toward the soma and proximal dendrites.

To examine more directly the temporal relationship between EPSPs and the K^+ currents that they activate, we isolated I_{K-LVA} in whole-cell recordings from MSO principal neurons at near-physiological temperature (35°C , see Online Methods), and delivered sEPSP commands that were scaled to produce depolarizations traversing the voltage range above -60 mV (peak amplitudes between -58 and -20 mV

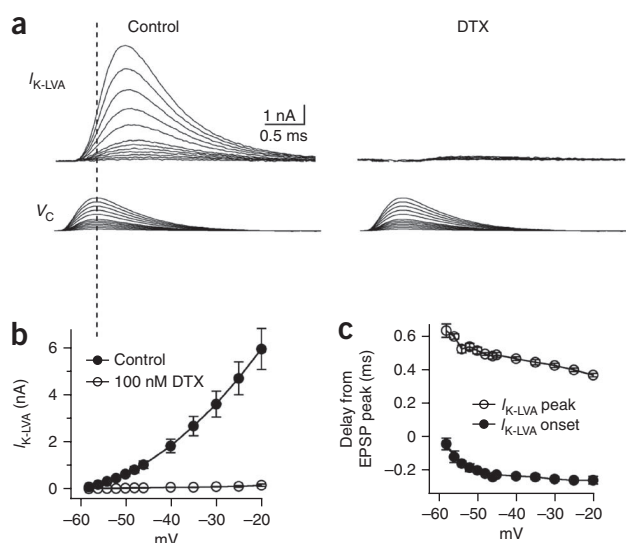


Figure 5 Relative timing of I_{K-LVA} and sEPSPs in whole-cell recordings at 35 °C. **(a)** I_{K-LVA} elicited by sEPSP voltage commands of amplitudes over the voltage range dominated by DTX-sensitive currents. sEPSP commands were delivered from the presumed resting membrane potential of -60 mV (see Online Methods for leak subtraction). The peak EPSP amplitudes were scaled between 2 and 40 mV with 2- or 5-mV intervals, corresponding to peak voltages between -58 and -20 mV. **(b)** Sensitivity of outward currents to 100 nM DTX ($n = 6$). **(c)** The time difference between the sEPSP peak and I_{K-LVA} onset (closed circle) and peak (open circle) is plotted as a function of peak membrane potential.

in 2- or 5-mV increments; **Fig. 5a,b** and Online Methods). In these experiments, a larger fraction of the current was sensitive to bath application of 100 nM DTX, as compared with responses to steps in outside-out patches (87–97% block between -60 and -20 mV, data not shown), possibly because the sEPSP commands were too brief to effectively activate slower currents that are not DTX sensitive. At all voltages, sEPSP commands elicited fast and transient outward currents whose peaks trailed the sEPSP peaks by 0.37–0.63 ms, depending on stimulus amplitude (**Fig. 5c**). The earliest discernable current (the onset, defined as the earliest outward current exceeding 3 s.d. above the noise floor of the recording) preceded the peak of the sEPSP command by only 0.04–0.26 ms. These results indicate that I_{K-LVA} possesses the appropriate properties to account for the voltage dependence and temporal dynamics of EPSP sharpening in MSO neurons. Notably, when the voltage-dependence of K_{LVA} was examined at 35 °C in whole-cell recordings using pharmacological subtractions, the half-activation voltage measured with single Boltzmann fits

was 11 mV more positive than that recorded in outside-out patches (**Supplementary Fig. 2**), a shift that could possibly reflect changes in the intracellular milieu and channel properties caused by patch excision that have been well documented (for example, see ref. 17). However, channel kinetics were similar between currents measured in whole-cell recordings and excised patches when the latter were corrected for their difference in temperature. As detailed below, successful reproduction of VDS in model MSO neurons required I_{K-LVA} activation to exhibit a voltage dependence that was closer to whole-cell rather than excised-patch parameters.

To better understand how EPSP sharpening is influenced by cell morphology and input location, we constructed an idealized compartmental model that describes the subthreshold nonlinear dynamics

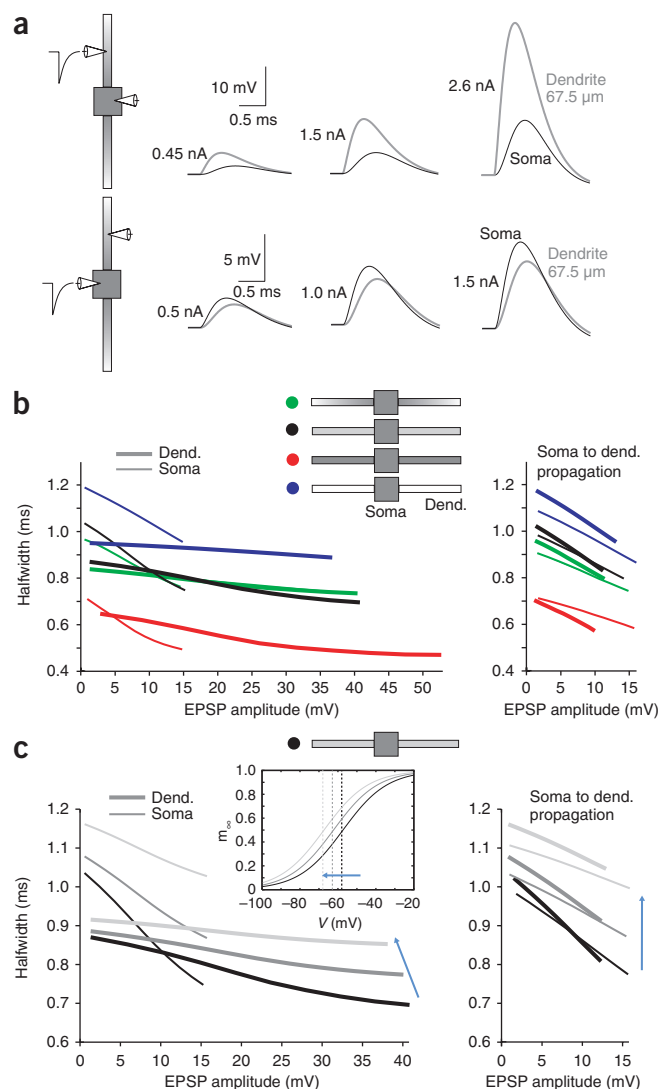
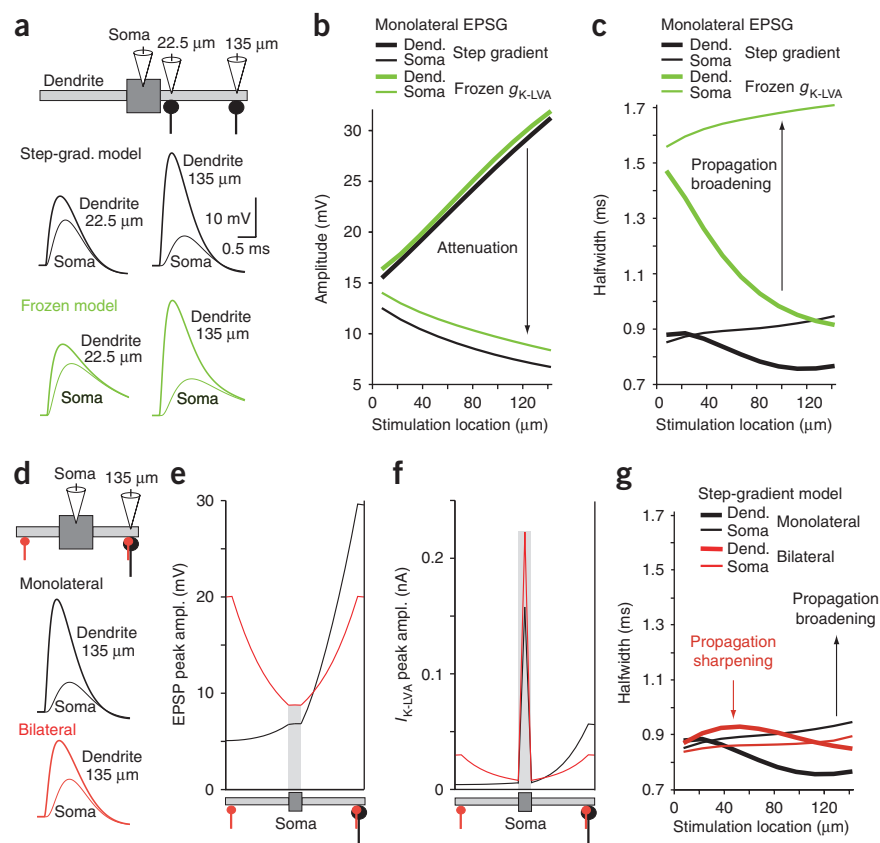


Figure 6 VDS for dendritic and somatic EPSC injection in a compartmental model of the MSO. **(a)** Schematic of dual recordings in the multicompartiment model. EPSCs were injected either in the dendrite 67.5 μm from the soma (top) or at the soma itself (bottom). Somatic EPSP halfwidth decreased as depolarization increased for both stimulus locations. **(b)** VDS dependence on the spatial distribution of K_{LVA} . VDS at the soma and at 67.5 μm in the dendrites (thin and thick lines) in response to either dendritic or somatic EPSCs (left and right, respectively). Four different I_{K-LVA} density distributions were compared. The green line indicates the exponential-gradient in dendritic I_{K-LVA} density based on experimental data (see **Fig. 4f,g**), the black line indicates the step-gradient model, the red line indicates the uniform I_{K-LVA} density and the blue line indicates active soma and passive dendrites with G_{K-LVA} in dendrites frozen at its resting value. The step-gradient model and exponential-gradient model best reproduce the experimental data presented in **Figure 1**. **(c)** Step-gradient model showing the dependence of VDS on the position of the I_{K-LVA} activation function. The left and right graphs show the dendritic and somatic sites of current injection, respectively. Inset, activation functions, $(m_{\infty})^4$, exhibited the same slopes, but different voltages of half-activation (black, $V_{1/2,m} = -58$ mV (as in whole-cell data); medium gray, $V_{1/2,m} = -63$ mV; light gray, $V_{1/2,m} = -68$ mV (as in outside-out patch data)). $V_{1/2,m}$ values correspond to single Boltzmann fits of maximal conductance adjusted to give the same resting conductance and potential for soma and dendrite in all three cases (**Supplementary Fig. 5**). The best match to the VDS data was obtained with $V_{1/2,m} = -58$ mV.

Figure 7 Spatial effects of VDS in an MSO neuron model. **(a)** Effect of I_{K-LVA} on EPSPs propagating through dendrites compared in models with active and passive g_{K-LVA} (step-gradient model and frozen model; black and green traces, respectively). Responses shown from two synaptic locations. **(b)** Dendritic and somatic EPSP amplitudes (thick and thin lines) as a function of dendritic EPSC location. EPSP amplitude attenuated from stimulation location to soma as predicted by cable theory. Models are color coded as in **a**. **(c)** Duration (halfwidth) of the dendritic and somatic EPSPs in **b**. EPSPs broadened for most of the synaptic locations in both models as predicted by cable theory. I_{K-LVA} generated more attenuation but also decreased EPSP broadening during propagation to the soma. **(d)** Comparison of VDS between monolateral and bilateral synaptic inputs 135 μm from the soma. Top, monolateral and bilateral configuration. Conductance in the monolateral case was double that of each bilateral synaptic input. Bottom, time courses for selected locations for monolateral and bilateral stimulation configurations. **(e)** Peak EPSP amplitude during propagation from the synaptic location to the soma. Stimulation occurred at 135 μm from the soma edge for monolateral and bilateral cases. **(f)** Peak I_{K-LVA} amplitude induced by EPSPs traveling from the stimulation location to the soma. **(g)** EPSP halfwidths for EPSPs recorded locally at the injection site in the dendrites (thick lines) and after propagation to the soma (thin lines). EPSPs broadened during propagation to the soma for most monolateral locations but sharpened for most bilateral locations.



of MSO principal neurons. The neuron model consists of a soma (a cylinder 20 μm long and 20 μm in diameter) and two unbranched dendrites (150 μm long and a uniform 3.5- μm diameter) in a bipolar configuration. The intrinsic properties were formulated according to the model ref. 18 with two modifications: the density of I_{K-LVA} and hyperpolarization-activated cation current (I_h) provided the majority of the resting conductance and the densities were adjusted to maintain a resting potential of -60 mV with a membrane time constant of 600 μs (see Online Methods and **Supplementary Fig. 3**). A lower density of dendritic versus somatic I_{K-LVA} was required to reproduce the pattern of VDS observed with forward propagating and backpropagating EPSPs. Models exhibiting either a uniform lower dendritic density of I_{K-LVA} (step-gradient model) or an exponentially declining gradient of dendritic I_{K-LVA} (exponential model) produced both the sensitive VDS at the soma and the relatively modest VDS observed during EPSP propagation into the dendrites (**Fig. 6a,b**). When a uniform density of I_{K-LVA} was employed throughout the soma and dendrites, VDS for backpropagating EPSPs was more pronounced in the dendrites than at the soma, contrary to experimental observations (**Fig. 6b**). Finally, in models in which dendritic I_{K-LVA} was replaced with a passive leak current (thus preserving the resting potential and time constant), VDS shifted to longer durations by ~ 200 μs . All models exhibited relatively modest VDS at their dendritic input sites as compared with the soma (**Fig. 6b**), which was a consequence of the relatively lower membrane surface area in the dendrites.

The relationship between the resting potential and I_{K-LVA} activation characteristics was a critical determinant of the maximum magnitude of VDS. In models, we observed the closest match with experimental VDS when I_{K-LVA} exhibited voltage dependence close to

what we observed in whole-cell experiments. With shallower activation functions, VDS was not as large as that observed experimentally (**Supplementary Fig. 4**). Shifts in I_{K-LVA} activation to progressively more negative voltages (such as the range observed in outside-out patches) resulted in a proportionally greater resting activation of the channel, but also led to a sharply reduced VDS of sEPSPs (**Fig. 6c** and **Supplementary Fig. 5**). These results suggest that the whole-cell configuration more closely maintains the native state of I_{K-LVA} and it was used in the model in subsequent simulations.

Additional insight into how I_{K-LVA} shapes EPSPs spatially was obtained with the model by simulating the responses to transient synaptic conductances of constant amplitude (EPSPs) injected at different dendritic locations. To further highlight the dynamic and nonlinear aspects of I_{K-LVA} activation, we carried out comparison simulations with the channel converted into a static conductance (frozen g_{K-LVA} ; **Fig. 7**). Increasingly larger local depolarizations were found for inputs that were more distant from the relatively large capacitance and current sink of the soma (**Fig. 7a,b**). With either active or frozen g_{K-LVA} , EPSPs at the soma exhibited progressively stronger attenuation as their stimulation distance increased. However, active g_{K-LVA} strongly regulated the duration of EPSPs all along the dendrite (**Fig. 7a,c**). In the model with frozen g_{K-LVA} , local dendritic EPSP duration decreased as synapse location moved distally as a result of the bipolar dendritic geometry (for example, EPSPs at the terminus of the dendrite will be briefer in a longer dendrite because depolarizing currents spread away comparatively faster). However, the relatively brief distal dendritic EPSPs broadened up to ~ 800 μs after propagation to soma as a result of passive cable filtering along the length of the dendrite. In models with active g_{K-LVA} , the temporal broadening of EPSP duration that

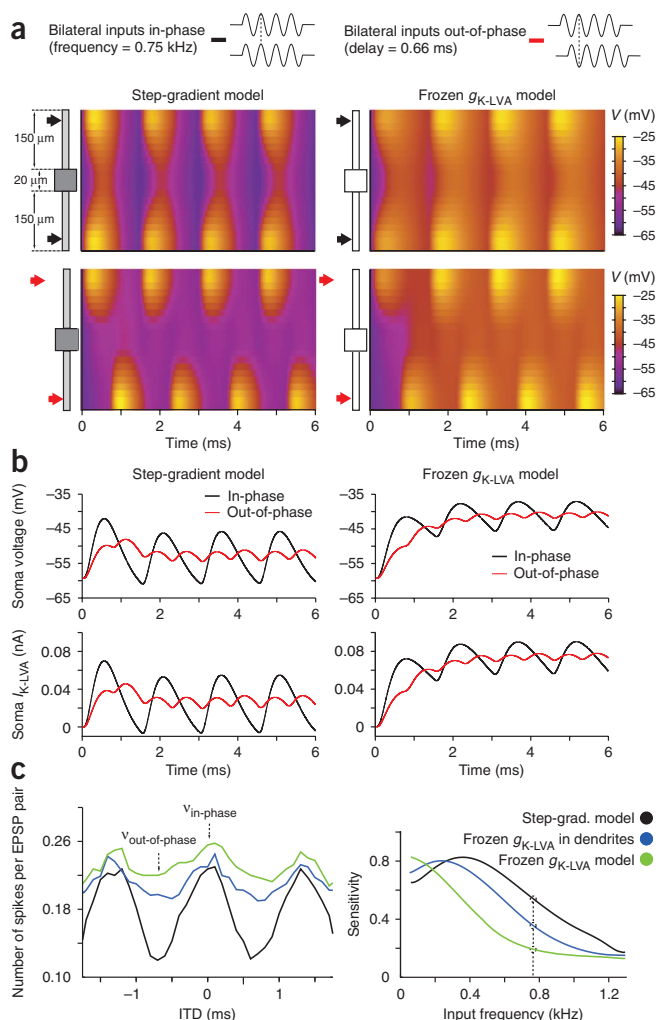


Figure 8 Spatio-temporal dynamics of membrane potential and I_{K-LVA} for bilateral ITD-like distal inputs (750 Hz). (a) Top, spatial profile of voltage along the soma and dendrites (ordinate) advancing in time for in-phase inputs. Color code indicates voltage. Step-gradient configuration is shown for active (left) and frozen g_{K-LVA} (right). Bottom, spatio-temporal voltage evolution for out-of-phase inputs. Active I_{K-LVA} sharpened voltage time courses, especially proximally. (b) Somatic voltage and I_{K-LVA} (top and bottom) time courses for in-phase (black) and out-of-phase (red) bilateral inputs. Left, step-gradient model with active g_{K-LVA} . Right, frozen g_{K-LVA} model, with I_{K-LVA} behaving as a leak current. (c) ITD-tuning curves and sensitivity function for three different spiking models (see Online Methods and **Supplementary Fig. 7**): step-gradient model (black), frozen g_{K-LVA} in dendrites (blue) and frozen g_{K-LVA} in the whole cell (green). Left, ITD-tuning curve for bilateral inputs at 750 Hz computed as v (the number of spikes per EPSP pair). For inputs at 750 Hz, the ratio of $v_{in-phase}$ to $v_{out-of-phase}$ for a model with frozen I_{K-LVA} was small, poorly discriminating different ITDs. The difference in number of spikes between in-phase inputs versus out-of-phase inputs increased as the amount of active I_{K-LVA} in the model increased (from green to blue to black curve). Right, sensitivity functions for different input frequencies in the MSO neurons' physiological range. The step-gradient model with a distribution of I_{K-LVA} similar to that found *in vitro* showed higher sensitivity for a broader range of input frequencies.

repetitive stimulation. We compared two models containing identical step-gradients of active or frozen g_{K-LVA} to either in-phase or out-of-phase bilateral excitatory inputs (**Fig. 8a**). The inputs that we delivered were short trains of synaptic conductances at 750 Hz (ten cycles with a period of ~ 1.3 ms). At such short interstimulus intervals, the onset of ongoing EPSPs would be in close temporal register with activated I_{K-LVA} . Compared with the active model, the frozen model showed an increase in temporal summation with reduced phase sensitivity at the soma for bilateral inputs (**Fig. 8b**) and less spatial attenuation of ongoing EPSPs throughout the cell (**Fig. 8a**). Active g_{K-LVA} far more effectively interacted with the temporal dynamics of each phase of somatic voltage changes, whereas frozen g_{K-LVA} functioned effectively as a leak current under the same stimulus conditions (**Fig. 8b**). When the model was elaborated to include an axon (with spike-generator conductances as described in ref. 18; see Online Methods and **Supplementary Figs. 7 and 8**), the ITD responsiveness reflected the EPSP sharpening for trains of binaural inputs (**Fig. 8c**). When g_{K-LVA} in the dendrites or in the whole neuron was frozen, temporal summation increased in the case of out-of-phase ITD inputs (**Fig. 8b**), increasing the number of spikes per bilateral EPSP input pairs. We defined ITD

sensitivity as the modulation index $\frac{v_{in\ phase} - v_{out\ of\ phase}}{v_{in\ phase} + v_{out\ of\ phase}}$, where

v is the firing frequency. Sensitivity degraded as more of g_{K-LVA} was frozen (**Fig. 8c**). Increasing input frequency decreased ITD sensitivity in all three cases because the temporal summation increased firing for out-of-phase stimulation and saturated firing frequency for in-phase stimulation (**Supplementary Figs. 8 and 9**). Thus, active g_{K-LVA} in the soma and dendrites improves ITD sensitivity over a larger input-frequency range. These results underscore the fact that I_{K-LVA} controls the length of EPSP duration and the time window of binaural coincidence detection at high frequencies not only through its passive contribution to the low input resistance, but also via its voltage dependency.

DISCUSSION

Voltage transients propagating along passive dendrites suffer distortions in amplitude, rise time and duration. These distortions would probably be problematic for neurons that use temporal coding strategies,

occurred with passive cable filtering was strongly reduced as a result of the active repolarization of propagating EPSPs, particularly in the proximal dendrites and soma, where channel density is the greatest (**Supplementary Fig. 6**).

The input location invariance of somatic EPSP duration was particularly notable during bilateral synaptic stimulation, a configuration that more closely resembles *in vivo* conditions during binaural hearing (**Fig. 7d–g**). In the bilateral configuration, each dendritic conductance was half the amplitude of those in monolateral simulations, thus representing the same number of activated synapses. Despite the fact that the dendrite(s) received the largest depolarization in these simulations, the largest recruitment of I_{K-LVA} occurred at the soma because of its greater I_{K-LVA} density and membrane surface area (**Fig. 7f**). Relatively stronger recruitment of somatic I_{K-LVA} occurred in the bilateral condition. Even though the input dendrite was more depolarized in the monolateral case, the opposite dendrite acted as a current sink, leading to less somatic depolarization. For the bilateral case, axial synaptic current from each dendrite meets at the soma, cancels and eliminates effective current spread into the opposite dendrite. Accordingly, bilaterally evoked somatic EPSPs exhibited shorter durations than monolateral EPSPs and showed less spatial dependence in duration (**Fig. 7g**).

The spatiotemporal influence of I_{K-LVA} on synaptic integration strongly enhanced the sensitivity of MSO neuron models to the submillisecond phase of excitatory inputs during high-frequency

as the location of the synapse itself would influence the timing of synaptic inputs at the soma and axon, and ultimately degrade the precision and reliability of action potential signaling. The encoding of sound-localization cues by MSO neurons represents one of the most marked examples of this paradox in the nervous system. Modulation of firing rate with changes in azimuthal sound location requires an ability to resolve time differences in the arrival of binaural inputs on the order of tens of microseconds, far shorter than the membrane time constant ($\sim 250 \mu\text{s}$ for adult animals)⁹. Our electrophysiological results and compartmental modeling indicate that both the biophysical properties and spatial distribution of K_v1 channels are essential for compensating for these passive cable distortions.

Molecular basis for I_{K-LVA}

We found that I_{K-LVA} is important for improving the time resolution of excitatory summation. In MSO principal neurons, channel activation occurred near -65 mV , which is negative to the average resting potential of -58 mV . The majority of K^+ currents at voltages negative to -30 mV was blocked by 100 nM DTX, a toxin that binds with high affinity to channels that possess $K_v1.1$, $K_v1.2$, $K_v1.3$ and $K_v1.6$ subunits¹⁹ variation range of the channel together with the sensitivity to dendrotoxin- $K^{9,15}$ is consistent with a heteromeric channel containing $K_v1.1$ subunits.

We observed a small DTX-insensitive component of low voltage-activate²¹. The negative acid outward current, consistent with physiological and behavioral studies showing that channels lacking $K_v1.1$ also influence auditory temporal coding^{22,23}. The kinetics of I_{K-LVA} that we determined in MSO neurons are considerably faster than those of homomeric K_v1 channels^{19,24} and resemble K_v1 channel kinetics that have been described in bushy cells of the mammalian cochlear nucleus¹⁸, which also encode auditory information with high temporal precision.

Synaptic sharpening by I_{K-LVA}

K_v1 channels are expressed throughout the CNS^{25,26}, where these channels provide a strong influence on both the current threshold for action potential initiation and the shape of the waveform itself^{27–30}. As a result of their activation in the subthreshold voltage range, K_v1 channels have been shown to dampen dendritic excitability and delay the onset of firing^{31–33}. Our results indicate that I_{K-LVA} is sufficiently rapid in MSO principal neurons to actively truncate the time course of synaptic excitation on a submillisecond timescale. Three features of I_{K-LVA} were critical for producing effective VDS in compartmental models. First, a steep voltage dependence of channel activation was important for the generation of substantial outward currents over the relatively limited ($\sim 12 \text{ mV}$) subthreshold voltage range of MSO neurons. Second, VDS was maximal in the compartmental model when we used the half-activation voltage obtained from whole-cell recordings and not that obtained from outside-out patches. Models with more negative ranges of channel activation increased the resting conductance, but exhibited comparatively little VDS. Third, the rapid kinetics of channel activation critically influenced the time course of excitation in the MSO. In whole-cell recordings, I_{K-LVA} accelerated the repolarization of sEPSPs, reducing the duration of dendritically propagated sEPSPs by as much as 46% (35% on average). It is important to consider that both leak and hyperpolarization-activated cation channels are also major components of the high intrinsic resolution of binaural coincidence detectors in birds and mammals, but their contribution to the overall resting conductance is static over the timescale of individual synaptic events³⁴. Along with K_{LVA} , these channels provide a fast overall response characteristic to MSO neurons, which is actively truncated by the additional recruitment of I_{K-LVA} during excitation.

K_v1 channels have long been known to be important for controlling the excitability and firing precision of neurons in auditory brainstem pathways concerned with temporal coding in both birds and mammals^{35–40}. As in the MSO, K_v1 channels in these neurons contribute substantially to the resting conductance, increasing the speed of membrane voltage changes, increasing the current required for action potential generation and suppressing repetitive firing^{41–43}. Our results, however, indicate that the contribution of K_v1 channels to the resting membrane properties in the MSO is, by itself, insufficient to provide the submillisecond temporal resolution required for ITD encoding. In models in which I_{K-LVA} was replaced with a passive leak current, the time course of excitation approximately doubled, which degraded the distinction between in-phase and out-of-phase bilateral excitation, especially at high frequencies (for example, Fig. 8). Thus, although it has been previously recognized that the activation of K_v1 channels is important for creating a narrow time window for action potential firing^{15,41–44}, our results highlight a far more dynamic role of K_v1 channels in defining the window over which binaural coincidence detection takes place.

Somato-dendritic distribution of I_{K-LVA}

To the best of our knowledge, our study is the first to examine how I_{K-LVA} acts spatially in the dendrites for the control of synaptic timing in the auditory system. We found that K_v1 channels are expressed in both the soma and dendrites, but their density is biased toward the soma. As EPSPs propagate along the dendrites of MSO principal neurons, passive cable filtering delays the rise time of EPSPs and increases their duration. However, as these events invade the proximal dendrites and soma, they differentially activate greater I_{K-LVA} near the soma as a result of the higher density of channels and the greater membrane surface area relative to the dendrites. In addition, the capacitive load of the soma prolongs excitation, resulting in more temporal overlap between I_{K-LVA} and the EPSP.

The perisomatic activation of I_{K-LVA} was particularly robust during bilateral stimulation, where slower, dendritically filtered EPSPs more efficiently recruited I_{K-LVA} proximally in opposing dendrites. Conversely, in the far distal dendrites, where cable properties dictated faster local EPSP time courses, we observed little effect of I_{K-LVA} -mediated EPSP sharpening even during strong depolarizations. Thus, the somatically biased distribution of I_{K-LVA} compensates for dendritic cable filtering and preserves the time course of submillisecond synaptic potentials occurring over disparate regions of the dendrites, effectively setting an upper limit on the duration of excitation.

Functional implications for ITD encoding *in vivo*

Extensive debate regarding models of ITD encoding revolves around whether the ITD sensitivity of MSO neurons is determined by the relative delays of excitatory binaural inputs (the Jeffress model)⁴⁵ or by the timing/and or magnitude of glycinergic inhibition (the Grothe/McAlpine model)^{46,47}. The role of I_{K-LVA} in shaping synaptic timing would be expected to affect all models of ITD detection, as the reduction of EPSP duration by I_{K-LVA} would increase the requirement for temporal proximity of binaural excitatory inputs and reduce the width of the ITD tuning curve, enabling a 'place code' to exist in the case of a Jeffress-type mechanism.

The width of excitatory tuning would influence a 'slope code' scenario that also features inhibition (Grothe/McAlpine model). However, the interactions of I_{K-LVA} with mixed inhibitory and excitatory synaptic potentials will likely be a more complicated function of their relative magnitudes and temporal patterns, neither of which have been described in MSO neurons *in vivo*. The location of the resting potential at the foot of the activation curve of I_{K-LVA} will render

the effects of this current highly sensitive to the effects of summing inhibition as well as neuromodulators that affect resting conductances. More generally, our results predict that I_{K-LVA} will be important for reducing firing to inappropriately timed excitation and enhancing the ability of MSO neurons to compute ITDs at higher frequencies.

METHODS

Methods and any associated references are available in the online version of the paper at <http://www.nature.com/natureneuroscience/>.

Note: Supplementary information is available on the Nature Neuroscience website.

ACKNOWLEDGMENTS

We thank D. Johnston and A. Reyes for their comments on a previous version of the manuscript. This work was supported by grants from the US National Institutes of Health (DC006877 to N.L.G. and DC008543 to J.R.) and Ruth Kirschstein National Research Service Awards to P.J.M. and L.L.S.

AUTHOR CONTRIBUTIONS

P.J.M. performed all of the voltage-clamp experiments characterizing I_{K-LVA} in patches and whole cells. N.L.G. conducted dual somatic and dendritic current-clamp recordings. L.L.S. performed some of the experiments from older animals and also made some of the initial observations on voltage-dependent sharpening. P.E.J. performed all of the simulations. N.L.G. and J.R. helped design and supervise the experiments and simulations, respectively. N.L.G. wrote the manuscript, with contributions from P.J.M., P.E.J. and J.R.

COMPETING FINANCIAL INTERESTS

The authors declare no competing financial interests.

Published online at <http://www.nature.com/natureneuroscience/>.

Reprints and permissions information is available online at <http://www.nature.com/reprintsandpermissions/>.

- Caporale, N. & Dan, Y. Spike timing-dependent plasticity: a Hebbian learning rule. *Annu. Rev. Neurosci.* **31**, 25–46 (2008).
- Mauk, M.D. & Buonomano, D.V. The neural basis of temporal processing. *Annu. Rev. Neurosci.* **27**, 307–340 (2004).
- Rinzel, J. & Rall, W. Transient response in a dendritic neuron model for current injected at one branch. *Biophys. J.* **14**, 759–790 (1974).
- Segev, I. & London, M. Untangling dendrites with quantitative models. *Science* **290**, 744–750 (2000).
- Carr, C.E. Processing of temporal information in the brain. *Annu. Rev. Neurosci.* **16**, 223–243 (1993).
- Grothe, B. Sensory systems: New roles for synaptic inhibition in sound localization. *Nat. Rev. Neurosci.* **4**, 540–550 (2003).
- Joris, P. & Yin, T. A matter of time: internal delays in binaural processing. *Trends Neurosci.* **30**, 70–78 (2007).
- Stotler, W.A. An experimental study of the cells and connections of the superior olivary complex of the cat. *J. Comp. Neurol.* **98**, 401–431 (1953).
- Scott, L.L., Mathews, P.J. & Golding, N.L. Posthearing developmental refinement of temporal processing in principal neurons of the medial superior olive. *J. Neurosci.* **25**, 7887–7895 (2005).
- Scott, L.L., Hage, T.A. & Golding, N.L. Weak action potential backpropagation is associated with high-frequency axonal firing capability in principal neurons of the gerbil medial superior olive. *J. Physiol. (Lond.)* **583**, 647–661 (2007).
- Agmon-Snir, H., Carr, C.E. & Rinzel, J. The role of dendrites in auditory coincidence detection. *Nature* **393**, 268–272 (1998).
- Dasika, V.K., White, J.A. & Colburn, H.S. Simple models show the general advantages of dendrites in coincidence detection. *J. Neurophysiol.* **97**, 3449–3459 (2007).
- Grau-Serrat, V., Carr, C.E. & Simon, J.Z. Modeling coincidence detection in nucleus laminaris. *Biol. Cybern.* **89**, 388–396 (2003).
- Zhou, Y., Carney, L.H. & Colburn, H.S. A model for interaural time difference sensitivity in the medial superior olive: interaction of excitatory and inhibitory synaptic inputs, channel dynamics and cellular morphology. *J. Neurosci.* **25**, 3046–3058 (2005).
- Svirskis, G., Kotak, V., Sanes, D.H. & Rinzel, J. Enhancement of signal-to-noise ratio and phase locking for small inputs by a low-threshold outward current in auditory neurons. *J. Neurosci.* **22**, 11019–11025 (2002).
- Scott, L.L., Mathews, P.J. & Golding, N.L. Perisomatic voltage-gated sodium channels actively maintain linear synaptic integration in principal neurons of the medial superior olive. *J. Neurosci.* **30**, 2039–2050 (2010).
- Martina, M., Vida, I. & Jonas, P. Distal initiation and active propagation of action potentials in interneuron dendrites. *Science* **287**, 295–300 (2000).
- Rothman, J.S. & Manis, P.B. Kinetic analyses of three distinct potassium conductances in ventral cochlear nucleus neurons. *J. Neurophysiol.* **89**, 3083–3096 (2003).
- Grissmer, S. *et al.* Pharmacological characterization of five cloned voltage-gated K⁺ channels, types Kv1.1, 1.2, 1.3, 1.5 and 3.1, stably expressed in mammalian cell lines. *Mol. Pharmacol.* **45**, 1227–1234 (1994).
- Hopkins, W.F., Allen, M.L., Houamed, K.M. & Tempel, B.L. Properties of voltage-gated K⁺ currents expressed in *Xenopus* oocytes by mKv1.1, mKv1.2 and their heteromultimers as revealed by mutagenesis of the dendrotoxin-binding site in mKv1.1. *Pflügers Arch.* **428**, 382–390 (1994).
- Stühmer, W. *et al.* Molecular basis of functional diversity of voltage-gated potassium channels in mammalian brain. *EMBO J.* **8**, 3235–3244 (1989).
- Allen, P.D., Schmuck, N., Ison, J.R. & Walton, J.P. Kv1.1 channel subunits are not necessary for high temporal acuity in behavioral and electrophysiological gap detection. *Hear. Res.* **246**, 52–58 (2008).
- Brew, H.M., Hallows, J.L. & Tempel, B.L. Hyperexcitability and reduced low threshold potassium currents in auditory neurons of mice lacking the channel subunit Kv1.1. *J. Physiol. (Lond.)* **548**, 1–20 (2003).
- Sokolov, M.V., Shamotoienko, O., Dhochartaigh, S.N., Sack, J.T. & Dolly, J.O. Concatemers of brain Kv1 channel alpha subunits that give similar K⁺ currents yield pharmacologically distinguishable heteromers. *Neuropharmacology* **53**, 272–282 (2007).
- Sheng, M., Tsaur, M.L., Jan, Y.N. & Jan, L.Y. Contrasting subcellular localization of the Kv1.2 K⁺ channel subunit in different neurons of rat brain. *J. Neurosci.* **14**, 2408–2417 (1994).
- Wang, H., Kunkel, D.D., Schwartzkroin, P.A. & Tempel, B.L. Localization of Kv1.1 and Kv1.2, two K channel proteins, to synaptic terminals, somata and dendrites in the mouse brain. *J. Neurosci.* **14**, 4588–4599 (1994).
- Bekkers, J.M. & Delaney, A.J. Modulation of excitability by alpha-dendrotoxin-sensitive potassium channels in neocortical pyramidal neurons. *J. Neurosci.* **21**, 6553–6560 (2001).
- Goldberg, E.M. *et al.* K⁺ channels at the axon initial segment dampen near-threshold excitability of neocortical fast-spiking GABAergic interneurons. *Neuron* **58**, 387–400 (2008).
- Kole, M.H., Letzkus, J.J. & Stuart, G.J. Axon initial segment Kv1 channels control axonal action potential waveform and synaptic efficacy. *Neuron* **55**, 633–647 (2007).
- Shu, Y., Yu, Y., Yang, J. & McCormick, D.A. Selective control of cortical axonal spikes by a slowly inactivating K⁺ current. *Proc. Natl. Acad. Sci. USA* **104**, 11453–11458 (2007).
- Mckay, B.E., Molineux, M.L., Mehaffey, W.H. & Turner, R.W. Kv1 K⁺ channels control Purkinje cell output to facilitate postsynaptic rebound discharge in deep cerebellar neurons. *J. Neurosci.* **25**, 1481–1492 (2005).
- Metz, A.E., Spruston, N. & Martina, M. Dendritic D-type potassium currents inhibit the spike afterdepolarization in rat hippocampal CA1 pyramidal neurons. *J. Physiol. (Lond.)* **581**, 175–187 (2007).
- Storm, J.F. Temporal integration by a slowly inactivating K⁺ current in hippocampal neurons. *Nature* **336**, 379–381 (1988).
- Yamada, R. Hyperpolarization-activated cyclic nucleotide-gated cation channels regulate auditory coincidence detection in nucleus laminaris of the chick. *J. Neurosci.* **25**, 8867–8877 (2005).
- Ashida, G., Abe, K., Funabiki, K. & Konishi, M. Passive soma facilitates submillisecond coincidence detection in the owl's auditory system. *J. Neurophysiol.* **97**, 2267–2282 (2007).
- Barnes-Davies, M., Barker, M.C., Osmani, F. & Forsythe, I.D. Kv1 currents mediate a gradient of principal neuron excitability across the tonotopic axis in the rat lateral superior olive. *Eur. J. Neurosci.* **19**, 325–333 (2004).
- Brew, H.M. & Forsythe, I.D. Two voltage-dependent K⁺ conductances with complementary functions in postsynaptic integration at a central auditory synapse. *J. Neurosci.* **15**, 8011–8022 (1995).
- Oertel, D., Bal, R., Gardner, S.M., Smith, P.H. & Joris, P.X. Detection of synchrony in the activity of auditory nerve fibers by octopus cells of the mammalian cochlear nucleus. *Proc. Natl. Acad. Sci. USA* **97**, 11773–11779 (2000).
- Reyes, A.D., Rubel, E.W. & Spain, W.J. Membrane properties underlying the firing of neurons in the avian cochlear nucleus. *J. Neurosci.* **14**, 5352–5364 (1994).
- Rothman, J.S. & Manis, P.B. The roles potassium currents play in regulating the electrical activity of ventral cochlear nucleus neurons. *J. Neurophysiol.* **89**, 3097–3113 (2003).
- Ferragamo, M.J. & Oertel, D. Octopus cells of the mammalian ventral cochlear nucleus sense the rate of depolarization. *J. Neurophysiol.* **87**, 2262–2270 (2002).
- Rathouz, M. & Trussell, L. Characterization of outward currents in neurons of the avian nucleus magnocellularis. *J. Neurophysiol.* **80**, 2824–2835 (1998).
- Svirskis, G., Kotak, V., Sanes, D.H. & Rinzel, J. Sodium along with low-threshold potassium currents enhance coincidence detection of subthreshold noisy signals in MSO neurons. *J. Neurophysiol.* **91**, 2465–2473 (2004).
- McGinley, M.J. & Oertel, D. Rate thresholds determine the precision of temporal integration in principal cells of the ventral cochlear nucleus. *Hear. Res.* **216–217**, 52–63 (2006).
- Jeffress, L.A. A place theory of sound localization. *J. Comp. Physiol. Psychol.* **41**, 35–39 (1948).
- Brand, A., Behrend, O., Marquardt, T., McAlpine, D. & Grothe, B. Precise inhibition is essential for microsecond interaural time difference coding. *Nature* **417**, 543–547 (2002).
- McAlpine, D., Jiang, D. & Palmer, A.R. A neural code for low-frequency sound localization in mammals. *Nat. Neurosci.* **4**, 396–401 (2001).

ONLINE METHODS

All experimental procedures followed the guidelines of the US National Institutes of Health and were approved by the Institutional Animal Care and Use Committee at the University of Texas at Austin.

Slice preparation. Mongolian gerbils (*Meriones unguiculatus*) from P16–19 were obtained from Charles River Laboratories or an in-house colony. In a small subset of experiments, older gerbils were used (P28–P35). Gerbils were anesthetized with halothane, decapitated, and their brains were removed in ACSF at 32 °C and saturated with 95%/5% oxygen/carbon dioxide. ACSF contained 125 mM NaCl, 2.5 mM KCl, 2 mM CaCl₂, 20 mM NaHCO₃, 1.25 mM NaH₂PO₄ and 25 mM glucose (pH 7.4 with NaOH). Horizontal brainstem slices 200 μm thick were cut with an oscillating tissue slicer (Leica VT1000S) at 32 °C. Slices were incubated at 35 °C in oxygenated ACSF for at least 30 min, and held at 23–24 °C thereafter. For recording, slices were transferred to a recording chamber and constantly superfused with oxygenated ACSF at ~4 mL min⁻¹ and held at 35 ± 0.1 °C unless indicated otherwise.

Current-clamp electrophysiology. For recording, slices were visualized at 160× using infrared differential interference contrast microscopy in conjunction with a Newvicon tube camera system (NC-70, Dage-MTI). Both dendritic and somatic current-clamp recordings were made with thick-walled borosilicate glass pipettes (1.65 outer diameter), pulled to resistances of 3–4 MΩ (somatic electrodes) or 6–11 MΩ (dendritic electrodes). The pipette solution consisted of 115 mM potassium gluconate, 20 mM KCl, 10 mM sodium phosphocreatine, 0.5 mM EGTA, 4 mM MgATP and 0.3 mM NaGTP (pH 7.3 with KOH). Dual current-clamp recordings were made with a pair of amplifiers with a fast voltage-follower circuit (BVC-700, Dagan) and signals were low-pass filtered at 5 kHz, digitized and transferred to a Macintosh Power PC via an Instrutech ITC-18 interface (sampling rate 50 kHz). Data acquisition was controlled by custom macros programmed in IGOR-Pro (WaveMetrics).

Analysis. Measurements of dendritic distances were made relative to the center of the soma. Recordings were accepted for analysis if the series resistance in the dendrites and soma remained below 50 and 15 MΩ, respectively. In addition, dual somatic recordings were used to confirm that the time course of the current injection was not affected by the range of series resistances encountered in these experiments. Drugs and toxins were bath applied. Group data reflect the average ± s.e.m. Unless otherwise specified, a two-tailed Student's *t* test with equal variance assumption was used for statistical comparisons, with a significance criterion of 0.05.

Voltage-clamp electrophysiology. Dendritic and somatic outside-out patches were obtained at 25 °C using an Axopatch 200B amplifier (Molecular Devices). The internal solution was the same as that used in the whole-cell current-clamp experiments. Pipettes had 5–7 MΩ open tip resistances. Patches were held at -90 mV and currents were elicited by voltage steps to between -80 and -20 mV (corrected for a 10-mV junction potential). Potassium currents were pharmacologically isolated with bath application of a control solution consisting of 1 μM TTX, 200 μM CoCl₂, 50 μM ZD7288 and 1 mM TEA to block voltage-gated sodium, calcium, *I_h* and high voltage-activate K⁺ currents. To further isolate channels containing K_v1 subunits, we subtracted currents obtained in control experiments from currents produced after 100 nM DTX was applied to the patch at ~0.4 psi via a 100 μm in diameter flow pipe (microfil, WPI). To prevent DTX from contaminating the solution bathing the slice, we housed the flow pipe inside the lumen of a glass capillary that siphoned extracellular solution from the bath. Patches were then guided inside the lumen of the siphon in front of the DTX flow pipe. Traces were low-pass filtered online at 2–5 kHz, and measurements were made from the average of one to four repetitions. The data were fit with a Boltzmann equation of the form $f(V) = \frac{1}{1 + e^{-\frac{V - V_{1/2}}{k}}}$, where $V_{1/2}$ is the half-maximal voltage

and k is the slope factor. To measure steady-state inactivation, we delivered brief prepulses (-90 to -40 mV for 10 ms) to patches and measured peak tail currents between -60 and -120 mV. Fits were made to tails 300 μs to 15 ms after the step using the equation $f(t) = (A \pm Be^{-t/\tau_w})^4$. Measurements from outside-out patches of I_{K-LVA} density were carried out in the control solution stated above. Steps

were delivered from a holding potential of -80 to -45 mV, below the activation of high voltage-activated K⁺ channels (activation ~-30 mV, data not shown). Traces represent the average of 10–70 trials. To maintain patch uniformity, we restricted pipette resistances between 8 and 9 MΩ (outer diameter of ~1.8 μm at 160× magnification). There was no substantial correlation between tip resistance and I_{K-LVA} magnitude (Supplementary Fig. 10). Online pipette capacitance compensation was employed and leak subtraction was performed using a P/-4 subtraction protocol.

In experiments measuring I_{K-LVA} in response to sEPSPs (Fig. 5), whole-cell voltage-clamp protocols were carried out at near physiological temperatures (35 °C) in the control solution described above. In addition, 6-cyano-7-nitroquinoxaline-2,3-dione (10 μM) and strychnine (1 μM) were added to the bath to decrease fast glutamatergic and glycinergic currents. I_{K-LVA} was elicited with EPSP voltage commands between 2 and 40 mV from -60 mV, the average resting potential of MSO neurons. EPSP commands were taken from the average evoked EPSP (~2 mV) in a cell that exhibited the average EPSP halfwidth of P17 gerbils (0.64 ms). All traces represent averages of three to six trials and were low-pass filtered at 5 kHz. Capacitance neutralization and >75% series resistance compensation were employed. Pipettes were wrapped with Parafilm to reduce pipette capacitance. Leak subtraction was performed offline using a P/-4 protocol. However, the leak pulses were elicited from a holding potential of -80 mV, outside of the activation range of I_{K-LVA} , but still in the linear portion of the *I-V* relationship (when I_h was blocked pharmacologically). To minimize noise, we averaged 20 traces of leak current before subtraction.

Modeling. An idealized compartmental model of an MSO neuron was developed that exhibits the characteristic bipolar dendritic architecture of these cells. The neuron model has a soma (area, A_s) and two unbranched dendrites of uniform diameter d (3.5 μm) and of length l (150 μm). The current balance equations in the nonspiking regime take the form, for each dendrite ($0 \leq x \leq l$), of

$$C_m \frac{\partial V}{\partial t} = \frac{d}{4R_i} \frac{\partial^2 V}{\partial x^2} - G_{leak}(V - V_{leak}) - G_{K-LVA}(x)m^4h(V - V_K) - G_h(V - V_h) - I_{syn}(x, t)$$

and, for example, for the somatic compartment,

$$\frac{\pi d^2}{4R_i} \left(\frac{\partial V_1}{\partial x} \Big|_{x=0} + \frac{\partial V_2}{\partial x} \Big|_{x=0} \right) = A_s \left(C_m \frac{\partial V}{\partial t} + G_{leak,S}(V_S - V_{leak}) + G_{K-LVA,S}m^4h(V_S - V_{K-LVA}) + G_{h,S}(V_S - V_h) \right)$$

The subscripts S, 1 and 2 refer to the soma and each of the two dendrites (for simplicity, we dropped the subscripts in the cable equation and for the gating variables in the soma), R_i is the axial resistivity (200 Ω cm) and C_m is the membrane capacitance (0.9 μF cm⁻²). The dendrites have sealed distal ends, $\frac{\partial V}{\partial x} \Big|_{x=l} = 0$.

The values for the maximal conductance densities G_x and reversal potentials V_x are given below. The inwardly rectifying cationic conductance, G_h , was modeled as a static leak, as channel gating kinetics are at least tenfold slower than the time course of EPSPs in MSO neurons (S. Khurana and N.L. Golding, *Soc. Neurosci. Abstr.* 467.15, 2007). The dynamics for the gating variables (activation, m and inactivation, h) of I_{K-LVA} satisfy

$$\frac{dm}{dt} = \frac{m_{\infty}(V) - m}{\tau_m(V)} \text{ and } \frac{dh}{dt} = \frac{h_{\infty}(V) - h}{\tau_h(V)}$$

where $m_{\infty}(V) = \frac{1}{1 + e^{\frac{V - V_{1/2,m}}{k_m}}}$, $h_{\infty}(V) = \frac{1 - \zeta}{1 + e^{\frac{V - V_{1/2,h}}{k_h}}} + \zeta$,

$$\tau_m(V) = \frac{21.5}{\frac{V+60}{6e^{-7}} + 24e^{-\frac{V+60}{50.6}}} + 0.35 \text{ and } \tau_h(V) = \frac{170}{\frac{V+60}{5e^{-10}} + e^{-\frac{V+70}{8}}} + 10.7.$$

The values for parameters (in mV, $V_{1/2,m} = -57.34$, $k_m = -11.7$, $V_{1/2,h} = -67$, $k_h = 6.16$, $\zeta = 0.27$); and expressions for $\tau_m(V)$ and $\tau_h(V)$ were obtained using Neurofit⁴⁸ based on our outside-out patch voltage-clamp recordings; functional

expressions for $\tau_m(V)$ and $\tau_h(V)$ were then fit using a least-squares method. We used m^4 for conductance activation of I_{K-LVA} , the lowest power that provided a good fit to the data. The voltage dependence of gating from outside-out patch data was shifted by about 10 mV in the depolarizing direction (see **Figs. 4d, 6b** and **Supplementary Fig. 5**). Although this description was used in our model simulations, a power of 1 was used to describe the channel activation curves in **Figure 4d** to provide a more intuitive description of the channel $V_{1/2}$ and aid comparisons with other studies. Maximal conductances were constrained to maintain a resting potential of ~ -60 mV and a somatic membrane time constant of ~ 0.6 ms, both average values for MSO neurons from 17–18-d-old gerbils⁹. In addition, we adjusted the dendritic maximal conductances (for step-gradient and exponential-gradient distributions) to match the average VDS recorded experimentally in both the soma and dendrites >50 μ m from the soma ($n = 13$). We found that VDS properties were well described if we chose a dendritic membrane time constant of 1.6 ms. Satisfying all of the above requirements proved difficult and required a precise balance between I_{K-LVA} and I_h . Furthermore, VDS was highly sensitive to both the voltage dependence and kinetics of I_{K-LVA} . As a confirmatory and independent check on our model, we simulated the response to an EPSP-like clamp at the soma (**Fig. 5**) and found that the I_{K-LVA} transients from the model and the experimental recordings agreed (**Supplementary Fig. 3**). For the soma, $G_{leak,S} = 0.3$, $G_{K-LVA,S} = 17$ and $G_{h,S} = 0.86$; these were also used for the dendrites in the case of uniform density model (conductances in $mS\ cm^{-2}$). For the dendrites in the step-gradient model, $G_{leak} = 0.3$, $G_{K-LVA} = 3.58$ and $G_h = 0.18$. For the dendrites in the exponential-gradient model, $G_{leak} = 0.3$, $G_{K-LVA} = 17(0.6e^{\frac{-x}{74}} + 0.05)$ and $G_h = 0.86(0.6e^{\frac{-x}{74}} + 0.05)$. In all cases, $V_{leak} = -60$ mV, $V_K = -106$ mV and $V_h = -43$ mV. With these conductance values and cable architecture, our neuron model has an input resistance of $R_{input} \approx 11.4\ M\Omega$ (from the soma) and dendritic space constant $\lambda_D = 280\ \mu$ m for the step-gradient and frozen cases.

The input I_{syn} was specified as a depolarizing current injection (double exponential function with $\tau_{rise} = 0.22$ ms and $\tau_{decay} = 0.43$ ms) or as a conductance-based excitatory input, $G_{syn}(x, t)(V - V_{syn})$, with G_{syn} as an alpha function with $\tau_{syn} = 0.2$ ms and $V_{syn} = 0$ mV.

For the compartmental implementation, we used ten equally sized compartments for each dendrite, whereas the soma was represented as a cylinder (diameter and length of 20 μ m) using three equally sized compartments (for example, ref. 49). Our computer code was written in the C programming language. The differential equations of the model were integrated numerically using the fourth-order Runge-Kutta method (see ref. 49), using a time step of 0.0025 ms.

The spiking model (**Supplementary Fig. 7**) was constructed from the multi-compartment model of bipolar dendrites and a soma (explained above) by adding a five-compartment initial segment of uniform diameter d (2 μ m) and of length l (25 μ m), and a five-compartment with uniform diameter axon d (1 μ m) and of length l (100 μ m). G_{K-LVA} and G_h are frozen for the initial segment and axon, and any VDS in the spiking model is therefore generated at the dendrite and soma compartments. The only active currents in the initial segment and axon were the high threshold-activated potassium current and sodium current obtained from ref. 18. Because spike identification is not problematic in the axon, spike counting for ITD tuning curves was done at the first node of the axon (**Supplementary Fig. 7**).

To create realistic ITD curves, we injected trains of conductance-based inputs into the middle compartment of each dendrite with different delays. Bilateral input trains (ten EPSP pairings with Gaussian noise on the amplitudes, maintaining constant total-EPSP amplitude and peak EPSP timing cycle to cycle) triggered spikes with different probabilities dependent on the relative delay of bilateral EPSPs invading the axonal spike generation region (**Supplementary Fig. 8**). We generated 40 trials for each ITD with ten cycles of bilateral simulation per trial. The s.d. for the number of spikes were computed to see the variability on spike count for each of the neuron model configurations (thin lines on the ITD tuning curves on **Supplementary Figs. 8 and 9**).

48. Willms, A.R. NEUROFIT: software for fitting Hodgkin-Huxley models to voltage-clamp data. *J. Neurosci. Methods* **121**, 139–150 (2002).

49. Koch, C. & Segev, I. *Methods in Neuronal Modeling: from Ions to Networks* (MIT Press, Cambridge, Massachusetts, 1998).